

# Patterning of particulate films using Faraday waves

P. H. Wright and J. R. Saylor<sup>a)</sup>

*Department of Mechanical Engineering, Clemson University, Clemson, South Carolina 29634*

(Received 8 April 2003; accepted 11 June 2003)

Faraday waves were used to create a patterned particulate film on the surface of a glass substrate. The process involves deposition of a thin liquid film on the substrate, where the liquid is comprised of water and a concentrated suspension of particles. Faraday waves were created on the surface of the liquid film by subjecting the substrate and film to a vertical oscillation. Because the films are thin, the standing waves create velocity fluctuations that are not negligible near the substrate surface. As the particles in the liquid settled to the bottom, the flow field caused by the waves caused preferential particle deposition organized in a pattern determined by the Faraday wave field. Subsequent evaporation of the liquid film left a particulate film on the solid substrate that retained the pattern of the original wave field. We refer to these particulate films as Faraday films. The length scale of the patterns in these films was on the order of millimeters in the experiments described here. Use of higher frequency oscillations could permit the formation of Faraday films having smaller spatial scales. © 2003 American Institute of Physics. [DOI: 10.1063/1.1602936]

## I. INTRODUCTION

When a gas/liquid interface is subjected to a vertical oscillation, a parametric instability occurs that can create surface waves, called Faraday waves.<sup>1</sup> These are standing waves having a wave frequency  $f_w$  equal to one-half the driving frequency  $f_e$ . Faraday waves present a basic fluid mechanics problem that has been studied both experimentally and analytically.<sup>2-6</sup> Faraday waves are fairly easy to generate in the laboratory and have been used as a platform for the study of chaotic dynamics.<sup>7-10</sup> These waves have also been used to study transport phenomena in nonlinear systems.<sup>11,12</sup> A review can be found in Miles and Henderson.<sup>13</sup>

When the Faraday wavelength is small, the restoring force for the wave is predominantly surface tension, and gravity plays a negligible role. This occurs for wavelengths  $\lambda \leq 1.7$  cm for water. In this case, Faraday waves are examples of standing capillary waves and are a useful tool for studying the role that capillary waves play in oceanic transport processes as has been done, for example, by MacIntyre,<sup>14</sup> Szeri,<sup>15</sup> Saylor,<sup>16</sup> and Saylor and Handler.<sup>17,18</sup>

The wavelength of Faraday waves can be determined using the linear dispersion relationship<sup>19</sup>

$$c^2 = \left[ \frac{g\lambda}{2\pi} + \frac{\sigma}{\rho} \left( \frac{2\pi}{\lambda} \right) \right] \tanh \left( \frac{2\pi H}{\lambda} \right), \quad (1)$$

where  $c$  is the phase speed of the wave,  $\sigma$  is surface tension,  $g$  the gravitational acceleration,  $\lambda$  the wavelength,  $\rho$  the liquid density, and  $H$  the thickness of the liquid layer. Here it has been assumed that the density of the liquid is much greater than the density of the air above the liquid. By substituting  $c = \lambda f_w$  in the left hand side, where  $f_w$  is the frequency of the Faraday wave, a value for  $\lambda$  can be obtained. In the present investigation we deal with capillary waves

exclusively, and so the surface tension term in Eq. (1) dominates the gravitational term which is dropped giving

$$c^2 = \frac{\sigma}{\rho} \left( \frac{2\pi}{\lambda} \right) \tanh \left( \frac{2\pi H}{\lambda} \right). \quad (2)$$

In typical studies of Faraday waves, the liquid layer is made to be deep when compared to the wavelength. In such cases the approximation  $\tanh(2\pi H/\lambda) \sim 1$  is used. In the present study we consider thin liquid films where the liquid depth is comparable to or smaller than the wavelength. Hence the value of  $2\pi H/\lambda$  becomes small and  $\tanh(2\pi H/\lambda) \sim 2\pi H/\lambda$ . Using this approximation, Eq. (2) becomes

$$c^2 = \frac{\sigma}{\rho} \left( \frac{2\pi}{\lambda} \right)^2 H. \quad (3)$$

This is the shallow limit of the linear dispersion relationship for capillary waves.

A plot of the wavelength  $\lambda$  versus the wave frequency  $f_w$  is presented in Fig. 1. This plot was obtained using Eq. (3). Water was used as the liquid in this calculation. Values used for the relevant fluid properties were  $\rho = 1000$  kg/m<sup>3</sup> and surface tension  $\sigma = 0.0718$  N/m. Again, note that the Faraday wave frequency  $f_w$  is half the driving frequency. Hence, if the liquid film is vibrated at a frequency of 200 Hz, the wave frequency will be 100 Hz and, according to Fig. 1, the wavelength will be  $\sim 4$  mm.

Investigations of Faraday waves have been predominantly for the deep water case. However, recent work on Faraday waves for the shallow case has revealed that the parametric instability may transition from the usual subharmonic wave to a harmonic one.<sup>20,21</sup> In this situation, mode competition is also different from the deep water case, favoring a hexagonal, rather than a square pattern as the waves transition to a harmonic state.<sup>20-22</sup>

Regardless of the mechanism which causes Faraday waves, or of whether the waves are created by a harmonic or

<sup>a)</sup> Author to whom correspondence should be addressed; electronic mail: jrsaylor@ces.clemson.edu

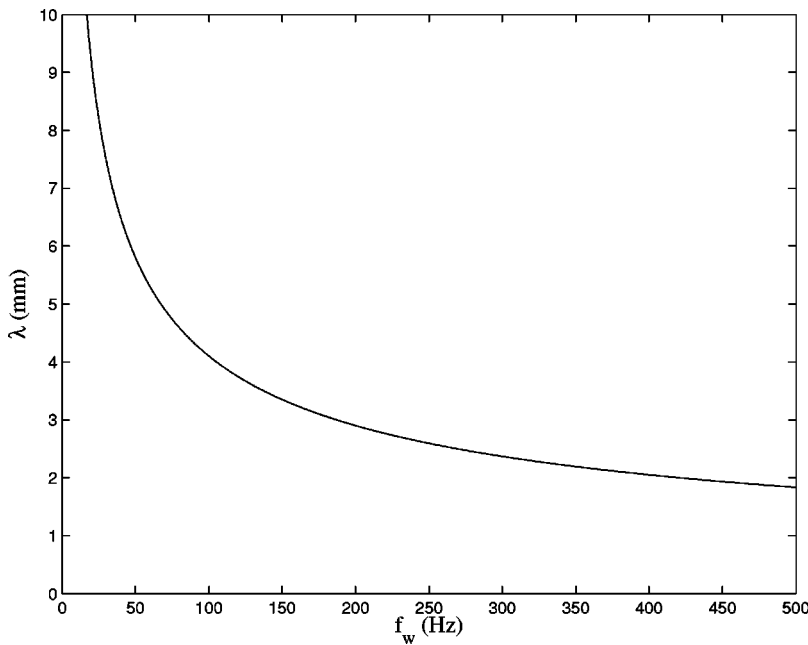


FIG. 1. Plot of wavelength vs wave frequency obtained from the linear dispersion relationship for the shallow limit of capillary waves. Liquid depth was set to 1 mm.

subharmonic parametric instability, the resulting waves are standing waves (for sufficiently small forcing amplitude). Faraday waves on thin liquid layers differ from their deep layer counterparts in that the wave motion results in significant fluid flow in the region near the bottom. This creates oscillating boundary layers which are used in the present work to enable control of particulate deposition on the surface of the substrate.

The second-order potential flow solution for the velocity field  $(u,v)$  and surface profile  $\eta$  of finite depth standing waves, developed by Miche<sup>23</sup> is

$$\begin{aligned}
 u(x,y) = & 2hb \frac{\cosh[a(H-y)]}{\sinh(aH)} \cos(ax) \cos(bt) \\
 & + \frac{3}{2} \frac{h^2 ab}{\sinh^4(aH)} \cosh[2a(H-y)] \\
 & \times \sin(2ax) \sin(2bt), \tag{4}
 \end{aligned}$$

$$\begin{aligned}
 v(x,y) = & -2hb \frac{\sinh[a(H-y)]}{\sinh(aH)} \sin(ax) \cos(bt) \\
 & + \frac{3}{2} \frac{h^2 ab}{\sinh^4(aH)} \sinh[2a(H-y)] \\
 & \times \cos(2ax) \sin(2bt), \tag{5}
 \end{aligned}$$

and

$$\begin{aligned}
 \eta(x) = & -2h \sin(ax) \sin(bt) + 2h^2 a \coth(aH) \cos(2ax) \\
 & \cdot \left[ \sin^2(bt) - \frac{3 \cos(2bt) + \tanh^2(aH)}{4 \sinh^2(aH)} \right], \tag{6}
 \end{aligned}$$

where  $H$  is the thickness of the liquid layer,  $2h$  is the wave amplitude,  $x$  is the lateral dimension,  $a=2\pi/\lambda$ ,  $\lambda$  is the wavelength,  $b=2\pi/\tau$ ,  $\tau$  is the wave period, and  $y=-z$  is the distance from the flat surface into the fluid ( $y$  is positive in the downward direction).

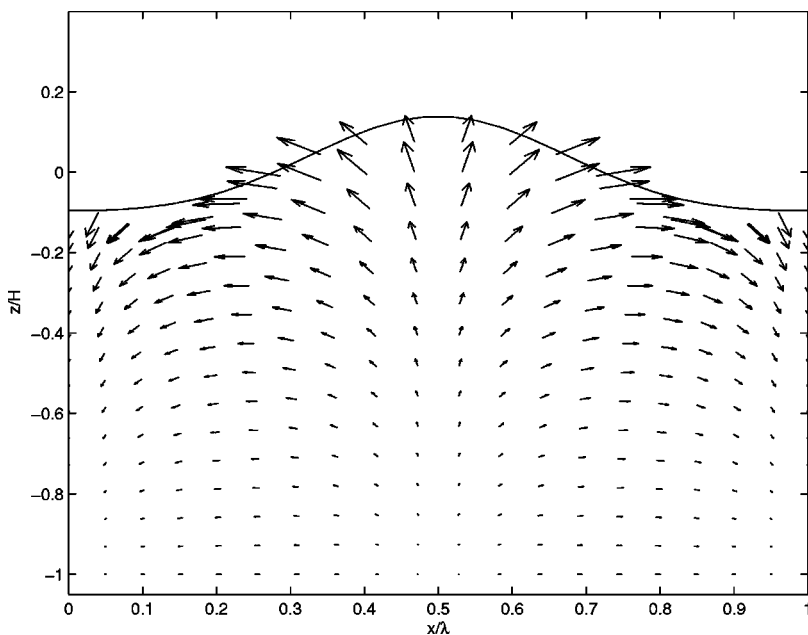


FIG. 2. Velocity field and wave profile for a standing wave using the second-order potential flow solution due to Miche (see Ref. 23).

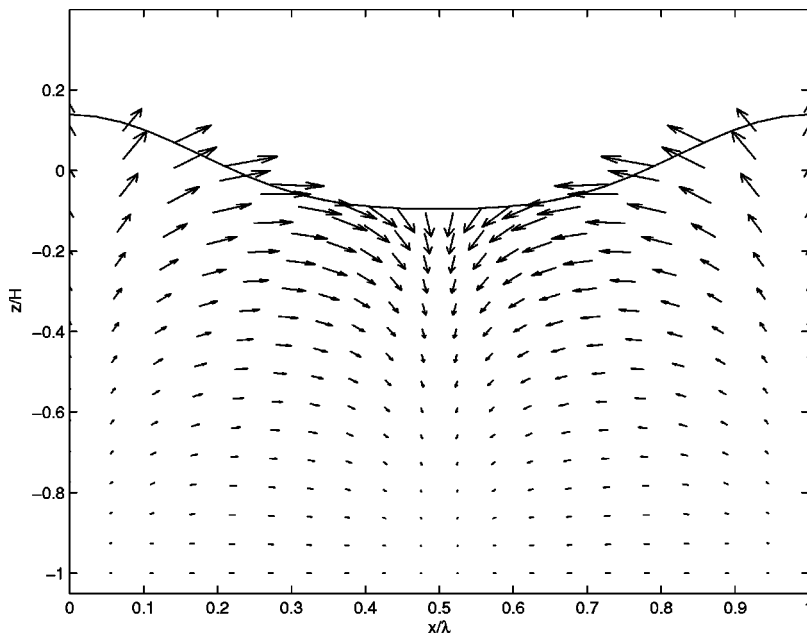


FIG. 3. Same as for Fig. 2, but 180° out of phase.

The velocity fields and wave profiles obtained from Eqs. (4)–(6) are presented in Figs. 2 and 3 for two instants in time separated by 180° in phase. These fields were obtained for the conditions  $H=0.5\lambda$  and  $h=0.05\lambda$ . These figures reveal the characteristic asymmetry in the wave profile; it is flatter in shape for the trough, and sharper in shape at the peak. The velocity fields reveal nonzero velocities at the solid substrate, a consequence of the inviscid solution. Although this nonzero velocity on the floor is nonphysical, the fact that these velocities are significant indicates that the boundary layers

which form at the bottom of these shallow waves will be robust.

Lin, Jeng, and Jeng<sup>24</sup> explored the boundary layers formed beneath standing waves in shallow liquid layers and developed a solution for the  $u$ -direction velocity field in these boundary layers. This solution permits the analysis of transport of particles that have fallen close to the solid surface. Based on the second-order inviscid solution due to Miche<sup>23</sup> and using the work of Noda,<sup>25</sup> Lin developed the following equation for  $u$  in the boundary layer:

$$\begin{aligned} \frac{u}{u_{\delta m}} = & -\sin(ax) \left[ \cos(bt) - e^{-z/\delta} \cos\left(bt - \frac{z}{\delta}\right) \right] + \frac{4h}{L} \left\{ \frac{-3\pi \cos(2ax)}{8 \sinh^3(aH)} \left[ \sin(2bt) - e^{-\sqrt{2}z/\delta} \sin\left(2bt - \sqrt{2} \frac{z}{\delta}\right) \right] \right. \\ & + \frac{\pi \sin(2ax)}{4 \sinh(aH)} \sin(2bt) \cdot \left[ e^{-\sqrt{2}z/\delta} \cos\left(\sqrt{2} \frac{z}{\delta}\right) - e^{-z/\delta} \cos\left(\frac{z}{\delta}\right) + \frac{\sqrt{2}z}{\delta} e^{-z/\delta} \sin\left(\frac{z}{\delta} + \frac{\pi}{4}\right) \right] + \frac{\pi \sin(2ax)}{4 \sinh(aH)} \cos(2bt) \\ & \cdot \left[ -e^{-\sqrt{2}z/\delta} \sin\left(\sqrt{2} \frac{z}{\delta}\right) + e^{-z/\delta} \sin\left(\frac{z}{\delta}\right) + \frac{\sqrt{2}z}{\delta} e^{-z/\delta} \cos\left(\frac{z}{\delta} + \frac{\pi}{4}\right) \right] + \frac{\pi \sin(2ax)}{8 \sinh(aH)} \left[ -3 + e^{-2z/\delta} + 8e^{-z/\delta} \sin\left(\frac{z}{\delta}\right) \right. \\ & \left. \left. + 2e^{-z/\delta} \cos\left(\frac{z}{\delta}\right) - 2\sqrt{2} \frac{z}{\delta} e^{-z/\delta} \cos\left(\frac{z}{\delta} + \frac{\pi}{4}\right) \right] \right\}. \end{aligned} \tag{7}$$

Here  $u_{\delta m}$  is the maximum velocity (the velocity outside the boundary layer)

$$u_{\delta m} = \frac{2bh}{\sinh(aH)}, \tag{8}$$

$\delta$  is the Stokes characteristic length

$$\delta = \sqrt{\frac{2\nu}{b}}, \tag{9}$$

$\nu$  is the kinematic viscosity, and  $z$  is the distance from the bottom boundary [note the sense of  $z$  is opposite that used in Eqs. (4)–(6)]. Equation (7) provides the oscillating boundary layer profile ( $u$  versus  $z$ ) at different lateral points beneath the wave. Plots of these oscillating boundary layer profiles are presented in Figs. 4 and 5 at  $x=\lambda/8$  and  $x=\lambda/2$ , respectively. In each figure, 40 velocity profiles are plotted over the course of a single wave period (only 20 are visible in Fig. 5 due to overlapping of the profiles during the wave period  $\tau$ ). An important characteristic of these plots is that the degree

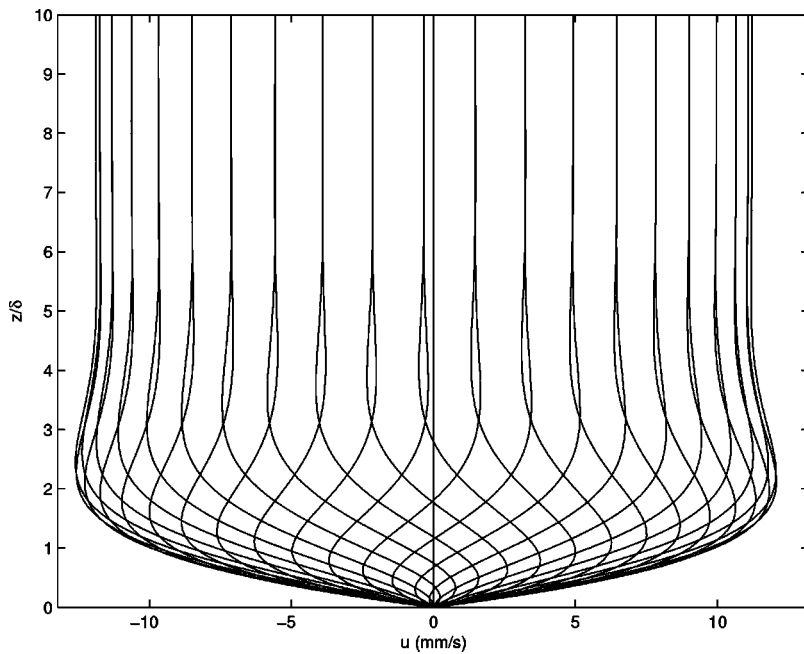


FIG. 4. Profiles of  $u$  as a function of  $z$  in the boundary layer for  $x=\lambda/8$ , obtained from Eq. (7). Forty profiles are presented, evenly spaced over a single wave period. Profiles obtained for the case of  $H=0.5\lambda$  and  $h=0.05\lambda$ .

of symmetry of the velocity profile with respect to time is different at these two  $x$  locations. Figure 5 indicates a very symmetric set of velocity profiles at  $x=\lambda/2$ . Hence, over the course of a single wave period the net flux of fluid is zero at this  $x$  location. However, the velocity profiles presented in Fig. 4 reveal an asymmetry about the vertical line. This can be seen especially at the extreme right and left hand sides of this figure where the peak velocities are different in the positive and negative directions. A consequence of this is a net flow in the negative direction for this particular  $x$  location. In Fig. 6 the net flow is plotted for a range of  $x$  locations spanning a single wavelength. The net flow values plotted in this figure were obtained by integrating the velocity profile at each  $x$  over a  $z$  domain from 0 to  $10\delta$  and integrating over a

time domain consisting of one period in the wave cycle. A unit depth into the plane of the page is assumed.

Figure 6 shows that the net flow achieves a maximum negative value at  $x=\lambda/8$  and  $5\lambda/8$  and a maximum positive value at  $x=3\lambda/8$  and  $7\lambda/8$ . In such a situation, any sediment located in this boundary layer region would tend to be swept to locations where two conditions are met: (i) the net flow is zero, and (ii) a positive net flow exists to the left, and a negative net flow to the right. These conditions are satisfied at  $x=0, \lambda/2, \lambda, 3\lambda/2, \dots$ , which is the locus of accumulation points in the boundary layer. This accumulation behavior is not observed in thick liquid layers due to the dramatic decrease in boundary layer velocity with increasing liquid depth. For example, by increasing the liquid layer from  $H$

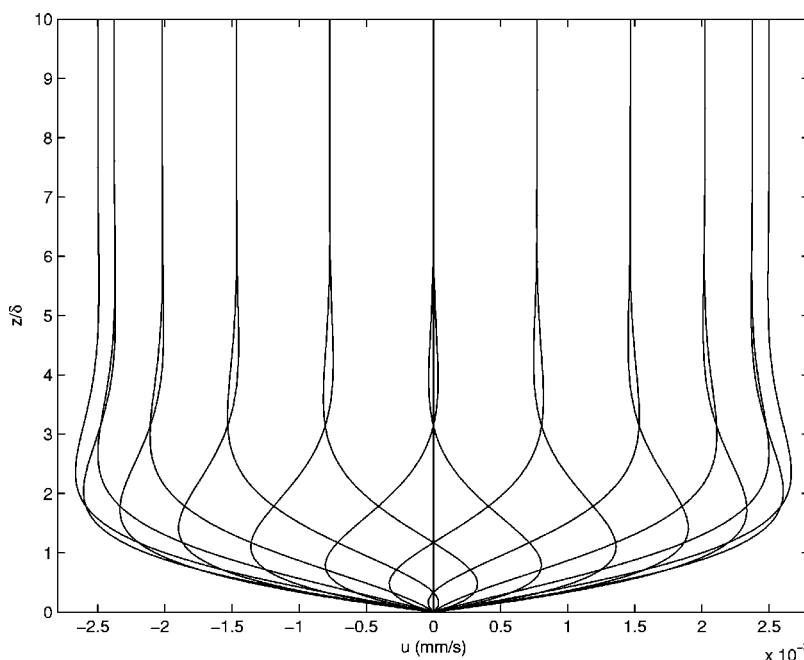


FIG. 5. Profiles of  $u$  as a function of  $z$  in the boundary layer for  $x=\lambda/2$ , obtained from Eq. (7). Forty profiles are presented, evenly spaced over a single wave period. Profiles obtained for the case of  $H=0.5\lambda$  and  $h=0.05\lambda$ .

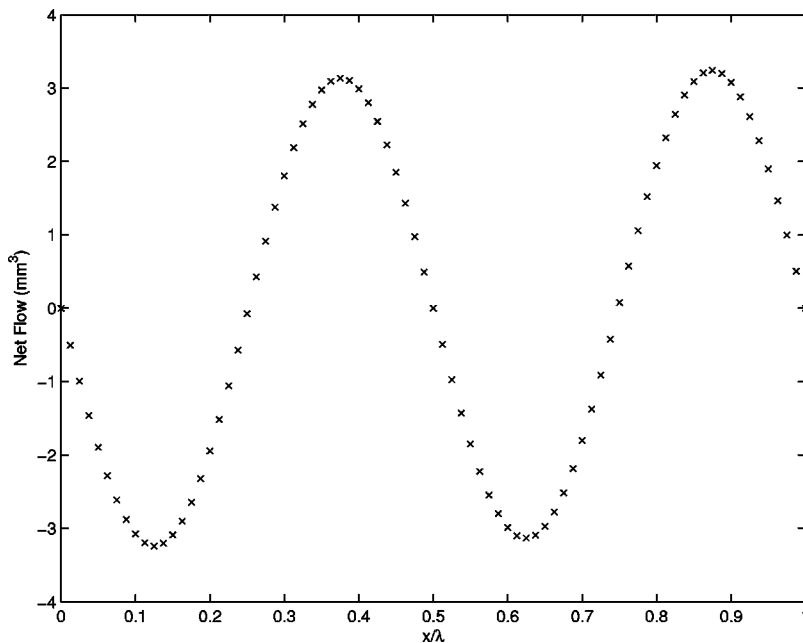


FIG. 6. Net fluid flow in  $\text{mm}^3$  occurring over a portion of the boundary layer from  $0 < z < 10\delta$  over a complete wave period, plotted against  $x$  ranging over one wavelength.  $H=0.5\lambda$  and  $h=0.05\lambda$ .

$=0.5\lambda$  to  $H=10\lambda$ , the magnitude of the peak velocities in Fig. 4 is decreased by a factor  $10^{22}$ , essentially eliminating this effect.

To demonstrate the ability of these wave induced oscillating boundary layers to cause particle accumulation at the specific locations indicated above, a simulation of particle transport was performed. Particles located in a grid just above the boundary layer were allowed to settle while being convected according to Eq. (7) which was numerically integrated using a time step equal to  $\pi/2560$ . The initial particle locations are seen in the uppermost frame of Fig. 7. The two frames below this show the particle locations after 200 and 400 wave cycles. The particles are seen to accumulate at the expected locations as they fall downward. The particle fall speed was adjusted so that all particles reached the bottom boundary before 400 wave cycles elapsed. The particles were convected at the exact local fluid velocity. Greater particle accumulation is observed as the fall speed decreases.

The characteristic of standing waves described above, where shallow thin films subjected to a standing wave field create oscillating boundary layers, was seen to be a useful method for controlling the deposition of particles. The accumulation points at specific nodes on the floor in the above simulations suggest that Faraday waves can be used to create rectilinear particulate patterns of controllable length scale. Such particulate patterns might be useful for a variety of applications in materials science, as well as in biomedical applications. Experiments designed to prove the feasibility of this particle deposition mechanism are now described.

## II. EXPERIMENTAL METHOD

The experimental apparatus used to generate Faraday waves consisted of an audio amplifier driven by a function generator (Simpson 420). The output from the amplifier was used to drive a 6W speaker. A glass microscope slide was covered with a thin film of the particulate/liquid mixture, and mounted in the center of the speaker cone. A small plastic

platform was glued onto the speaker cone to facilitate this. Four, 2 in. alligator clips were used to fix the microscope slide in place. A top view of the experimental apparatus is presented in Fig. 8.

The particulate/liquid mixture consisted of a commercially available, powdered talc mixed with doubly de-ionized water. Before use, the talc was mixed with isopropyl alcohol to dissolve fragrances and other organic compounds in the talc. After thoroughly mixing the talc and isopropyl alcohol in a beaker, the talc was allowed to settle to the bottom and the alcohol was then decanted. When as much of the isopropyl alcohol had been decanted as possible, the remainder was allowed to evaporate. The dried talc was then used to create the talc/water mixture.

The substrate upon which the talc/water mixture was placed consisted of a microscope slide. A 22 mm  $\times$  22 mm glass cover slip (VWR), was glued on top of the microscope slide to provide a slightly elevated platform on which to deposit the liquid film. This 22 mm  $\times$  22 mm region is the square region seen in the center of Fig. 8. When the talc/water mixture was deposited on the cover slip, the advancing meniscus would stop at the edge of the cover slip, creating a square, reproducible film.

The talc/water mixture was deposited using a dropper. The solution was vigorously mixed prior to deposition so that the talc was uniformly distributed in the water. The mixture was deposited onto the glass cover slip until the entire cover slip was covered with a liquid film. After initial deposition, the liquid film was typically too thick in that it exceeded the Faraday wavelength  $\lambda$ . To thin the film, excess moisture was wicked away by applying a laboratory tissue (Kimberly-Clark) to the edge of the film. Liquid was wicked away until the film thickness was smaller than or comparable to  $\lambda$ .

Once the talc/water film was properly established on the microscope slide a Faraday wave field was established on the

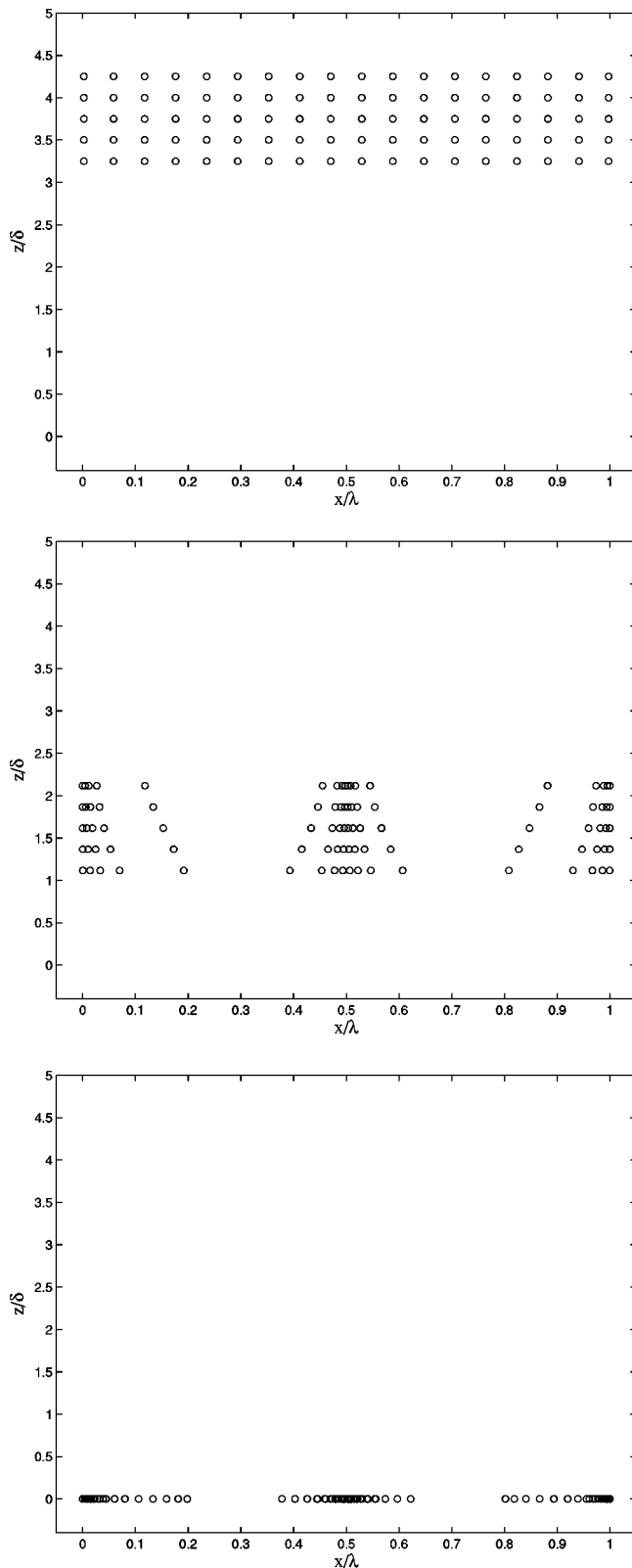


FIG. 7. Location of particles transported by the oscillating boundary layer as defined in Eq. (7). Uppermost frame shows the initial particle locations. The remaining two frames show the particle locations after 200 and 400 wave cycles. The fall velocity of the particles was set to a value of  $v = (4.3\delta)/(400\tau)$ . The relevant wave parameters are  $H = 0.5\lambda$  and  $h = 0.05\lambda$ .

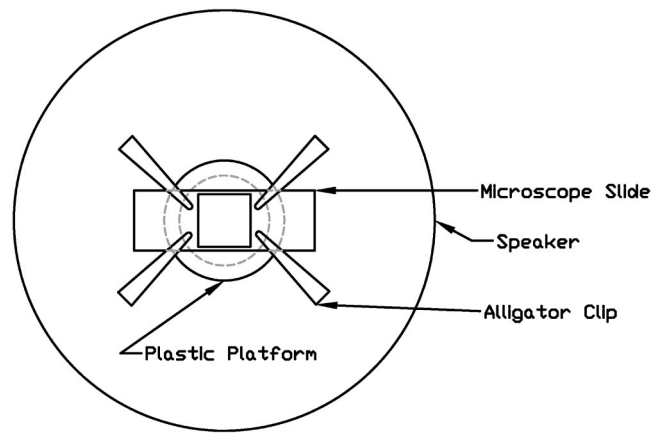


FIG. 8. Top view of experimental apparatus.

liquid surface by setting the frequency of the function generator, and then increasing the amplitude of the forcing using the audio amplifier until a wave field was observed. Due to hysteresis in forcing amplitude, the onset of Faraday waves usually occurred in the chaotic regime, and the standing wave field was observed to wander and acted only to mix the particles in the thin liquid film. To create a fixed standing wave field, the amplitude was slowly reduced until the field became stationary, with a pattern of nodes and anti-nodes observed in a rectilinear array oriented with the edges of the glass cover slip. The wave field was maintained until a pattern in the talc was observed to form on the bottom (the surface of the cover slip). The amplifier was then turned off and the film allowed to dry. For a typical film, particulate patterns were observed a few seconds after a stable Faraday wave field was formed. The drying time was typically around 8 h. The evaporation process did not seem to significantly change the observed particulate pattern.

A process of trial and error was used to determine the talc concentration that produced the best patterns. Table I shows the particulate concentrations in mg of talc per ml of water used at each excitation frequency.

### III. RESULTS

Digital photographs of the resulting films are presented in Figs. 9–13. Each frame contains the complete  $22\text{ mm} \times 22\text{ mm}$  extent of the glass cover slip. The wave pattern seen in these particulate Faraday films is very similar to that observed on the liquid surface when the Faraday waves were present.

The coherence of these wave patterns varies. At lower frequencies, the wavelengths are larger. This is helpful in the sense that the number of wave modes which can be accom-

TABLE I. Parameter space for experiments.

$f_e$ (Hz)	Concentration (mg/ml)	Corresponding figure
150	15	9
200	7.5	10
275	7.5	11
300	6	12
350	7.5	13

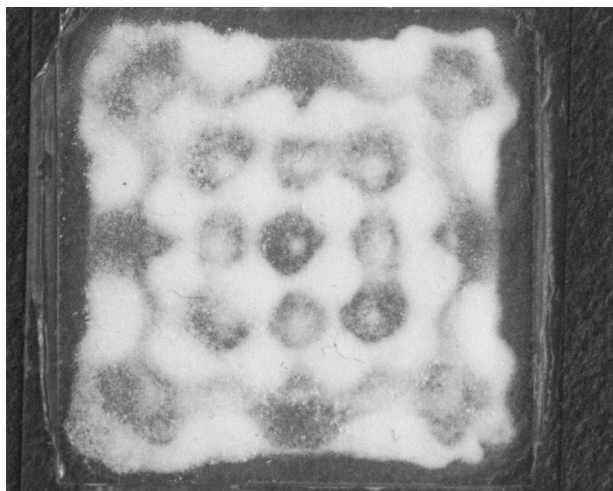


FIG. 9. Image of Faraday film created using an excitation frequency of 150 Hz.

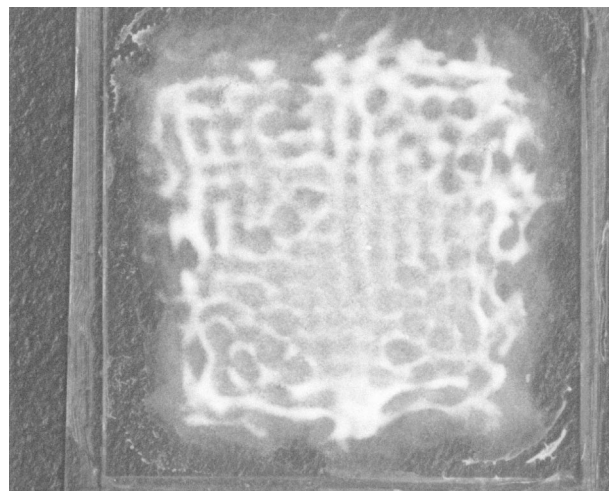


FIG. 12. Image of Faraday film created using an excitation frequency of 300 Hz.

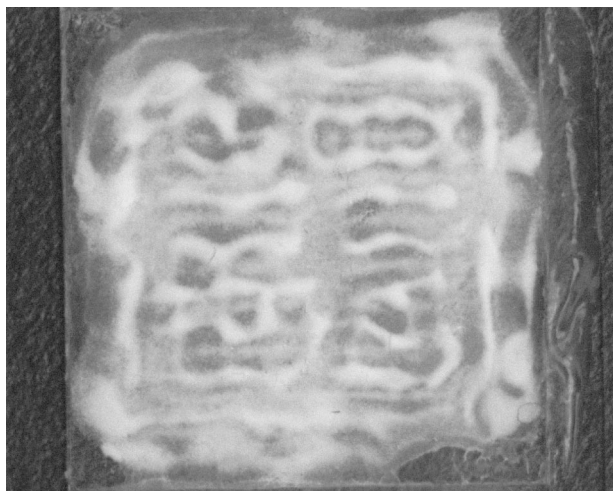


FIG. 10. Image of Faraday film created using an excitation frequency of 200 Hz.

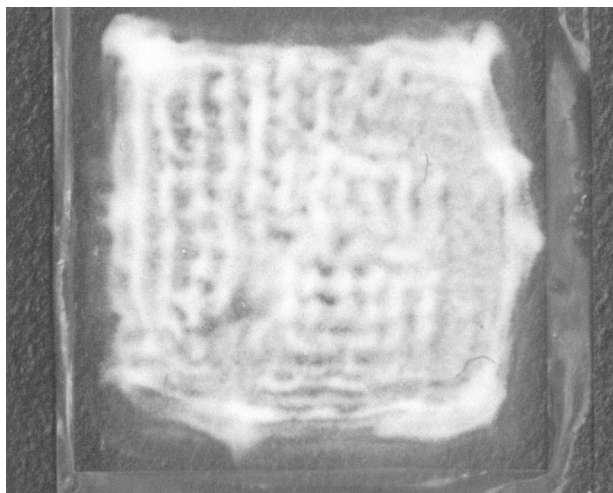


FIG. 11. Image of Faraday film created using an excitation frequency of 275 Hz.

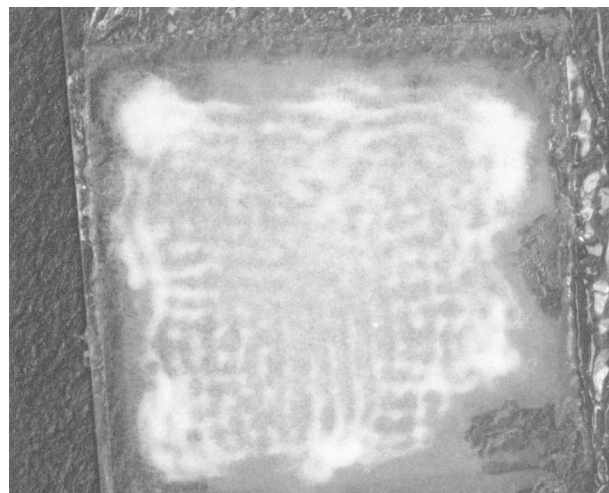


FIG. 13. Image of Faraday film created using an excitation frequency of 350 Hz.

modated on the expanse of the microscope slide is small. Hence there is less mode competition and the wave pattern appears more rectilinear in shape. As the frequency increases and the wavelength decreases in size, mode competition increases and the wave field is not as coherent. Although not attempted in this work, this effect can be eliminated by reducing the spatial extent of the film as the frequency is increased. Here, the spatial extent of the film was kept constant to make simple comparison of the different films.

In each of the images it can be seen that the edges of the particulate film do not coincide with the edges of the cover slip. This effect is not due to incomplete coverage of the cover slip by the liquid film. Rather, upon initiation of the Faraday wave field, the meniscus was observed to pull away from the edge of the cover slip. The reason for this is not clear, but it is the cause of the somewhat rounded edges of these Faraday films.

#### IV. DISCUSSION

The wavelengths of the patterns in the Faraday films presented in Figs. 9–13 are listed in Table II. The first

TABLE II. Comparison of measured wavelengths and expected wavelength.

$f_e$ (Hz)	$f_w$ (Hz)	$\lambda_m$ (mm)	$\lambda_p$ (mm)
150	75	8.0	4.7
200	100	4.4	4.1
275	138	3.2	3.5
300	150	2.8	3.35
350	175	2.0	3.1

column of this table is the excitation frequency  $f_e$ , the second is the wave frequency  $f_w$ , which is  $f_e/2$ . The third column is the measured wavelength of the particulate pattern  $\lambda_m$ , and the fourth column is the wavelength predicted by Eq. (3),  $\lambda_p$ . Note that according to Fig. 6 and the discussion presented in Sec. I, the distance between two accumulation points is  $\lambda/2$ . Hence, the value of  $\lambda_m$  in Table II is twice the distance between two regions where significant particulate accumulation is observed in the relevant figures.

There are significant discrepancies between  $\lambda_m$  and  $\lambda_p$ . Exactly why this is the case is not clear. As noted in the Introduction, prior researchers noted a switch from a subharmonic instability to a harmonic instability when the liquid layer gets sufficiently thin. If this occurs, then  $f_w = f_e$  instead of  $f_w = f_e/2$  as was assumed here, and the observed wavelengths would be smaller than predicted. This is in fact the case for  $f_e = 275 - 350$  Hz, however for the other frequencies  $\lambda_m$  is greater than  $\lambda_p$ . It may be the case that a transition to a harmonic instability occurred for the three highest frequencies, but not for the lower frequencies. Why there are such large deviations above the expected wavelengths for the low frequency cases is unclear. It is noted that the largest

deviation of  $\lambda_m$  from  $\lambda_p$  occurs for the largest wavelength. It is possible that for this case, where only about three wavelengths fit onto the cover slip, that edge effects cause some distortion of the wave field. This is especially possible due to the pulling-in of the meniscus which occurred during Faraday wave initiation.

- <sup>1</sup>M. Faraday, Philos. Trans. R. Soc. London **121**, 319 (1831).
- <sup>2</sup>T. B. Benjamin and F. Ursell, Proc. R. Soc. London, Ser. A **225**, 505 (1954).
- <sup>3</sup>J. W. Miles, J. Fluid Mech. **248**, 671 (1993).
- <sup>4</sup>D. M. Henderson and J. W. Miles, J. Fluid Mech. **213**, 95 (1990).
- <sup>5</sup>D. M. Henderson and J. W. Miles, J. Fluid Mech. **222**, 449 (1991).
- <sup>6</sup>D. M. Henderson, J. Fluid Mech. **365**, 89 (1998).
- <sup>7</sup>S. Ciliberto and J. P. Gollub, J. Fluid Mech. **158**, 381 (1985).
- <sup>8</sup>E. Meron and I. Procaccia, Phys. Rev. Lett. **56**, 1323 (1986).
- <sup>9</sup>E. Meron, Phys. Rev. A **35**, 4892 (1987).
- <sup>10</sup>F. Simonelli and J. P. Gollub, Rev. Sci. Instrum. **59**, 280 (1988).
- <sup>11</sup>R. Ramshankar, D. Berlin, and J. P. Gollub, Phys. Fluids A **2**, 1955 (1990).
- <sup>12</sup>R. Ramshankar and J. P. Gollub, Phys. Fluids A **3**, 1344 (1991).
- <sup>13</sup>J. W. Miles and D. M. Henderson, Annu. Rev. Fluid Mech. **22**, 143 (1990).
- <sup>14</sup>F. MacIntyre, Phys. Fluids **14**, 1596 (1971).
- <sup>15</sup>A. J. Szeri, R. L. Stefan, and J. R. Saylor, *Fluid Mechanics and the Environment: Dynamical Approaches*, Lecture Notes in Physics (Springer, Berlin, 2001).
- <sup>16</sup>J. R. Saylor, Tellus, Ser. B **51B**, 616 (1999).
- <sup>17</sup>J. R. Saylor and R. A. Handler, Exp. Fluids **27**, 332 (1999).
- <sup>18</sup>J. R. Saylor and R. A. Handler, Phys. Fluids **9**, 2529 (1997).
- <sup>19</sup>G. Dietrich, *General Oceanography* (Wiley, New York, 1963).
- <sup>20</sup>H. W. Müller, H. Wittmer, C. Wagner, J. Albers, and K. Knorr, Phys. Rev. Lett. **78**, 2357 (1997).
- <sup>21</sup>C. Wagner, H. W. Müller, and K. Knorr, Phys. Rev. E **62**, R33 (2000).
- <sup>22</sup>D. Binks, M.-T. Westra, and W. van de Water, Phys. Rev. Lett. **79**, 5010 (1997).
- <sup>23</sup>M. Miche, Ann. Ponts Chaussees **144**, 25 (1944).
- <sup>24</sup>C. Lin, D. S. Jeng, and C. N. Jeng, Ocean Eng. **29**, 1265 (2002).
- <sup>25</sup>H. Noda, in *Proceedings of the 11th International Conference on Coastal Engineering* (ASCE, London, 1968), pp. 227-247.